Journal of Structural Biology 213 (2021) 107700

Contents lists available at ScienceDirect

Journal of Structural Biology

journal homepage: www.elsevier.com/locate/yjsbi

Structural insights into novel mechanisms of inhibition of the major β-carbonic anhydrase CafB from the pathogenic fungus *Aspergillus fumigatus*

Subin Kim, Jungyoon Yeon, Jongmin Sung, Na Jin Kim, Semi Hong, Mi Sun Jin *

School of Life Sciences, GIST, 123 Cheomdan-gwagiro, Buk-gu, Gwangju 61005, Republic of Korea

ARTICLE INFO

Keywords:
β-class carbonic anhydrase
Zinc metalloenzyme
CafB
Aspergillus fumigatus
Oxidative inhibition
Zinc-free inactivation
X-ray crystallography

ABSTRACT

In fungi the β-class of carbonic anhydrases (β-CAs) are zinc metalloenzymes that are essential for growth, survival, differentiation, and virulence. *Aspergillus fumigatus* is the most important pathogen responsible for invasive aspergillosis and possesses two major β-CAs, CafA and CafB. Recently we reported the biochemical characterization and 1.8 Å crystal structure of CafA. Here, we report a crystallographic analysis of CafB revealing the mechanism of enzyme catalysis and establish the relationship of this enzyme to other β-CAs. While CafA has a typical open conformation, CafB, when exposed to acidic pH and/or an oxidative environment, has a novel type of active site in which a disulfide bond is formed between two zinc-ligating cysteines, expelling the zinc ion and stabilizing the inactive form of the enzyme. Based on the structural data, we generated an oxidation-resistant mutant (Y159A) of CafB. The crystal structure of the mutant under reducing conditions retains a catalytic zinc at the expected position, tetrahedrally coordinated by three residues (C57, H113 and C116) and an aspartic acid (D59), and replacing the zinc-bound water molecule in the closed form. Furthermore, the active site of CafB crystals grown under zinc-limiting conditions has a novel conformation in which the solvent-exposed catalytic cysteine (C116) is flipped out of the metal coordination sphere, facilitating release of the zinc ion. Taken together, our results suggest that *A. fumigatus* use sophisticated activity-inhibiting strategies to enhance its survival during infection.

1. Introduction

Carbonic anhydrases are ubiquitous zinc metalloenzymes that catalyze the rapid and reversible interconversion of carbon dioxide (CO_2) with bicarbonate (HCO_3^-) plus a proton (Supuran, 2016). They are broadly grouped into seven classes (α, β, γ, δ, ζ, η and θ) (Del Prete et al., 2014a, 2014b; Iverson et al., 2000; Kikutani et al., 2016; Meldrum and Roughton, 1933; Mitsuhashi et al., 2000; Xu et al., 2008). β-CAs are found in bacteria, archaea, fungi, algae and plants, but not in mammals (Neish, 1939; Smith et al., 1999). They are structurally distinct from the α-CAs of humans, and thus have been extensively studied with the aim of developing new antimicrobial agents (Supuran, 2008). They exist in various oligomeric states, including dimers, tetramers, hexamers, and octamers (Hiltonen et al., 1998; Kimber and Pai, 2000; Rumeau et al., 1996; Smith and Ferry, 1999; Kisiel and Graf, 1972), and mainly occur in two distinct zinc-binding states, denoted as the R-state (Type-I or open) and the T-state (Type-II or closed) (Rowlett, 2010). In the R-state, one histidine, two cysteines, and a water molecule coordinate the zinc ion in the active site. In the T-state, however, the water molecule is replaced with an aspartic acid residue, rendering this state catalytically inactive. Some bacterial β-CAs reportedly switch between these two states in a pH-dependent manner (Covarrubias et al., 2006; Suarez Covarrubias et al., 2005) or by allosteric binding of bicarbonate at a non-catalytic inhibitory site (Cronk et al., 2006; Ferraroni et al., 2015).

The majority of fungi possess multiple β-CAs, among which major and minor forms have been functionally characterized (Bahn et al., 2005; Elleuche and Pöggeler, 2009; Ren et al., 2014). The fungal pathogen *Aspergillus fumigatus* is the main causative agent of invasive aspergillosis and has four β-CA isoforms (CafA-D) that occupy different cellular locations and vary in efficiency (Han et al., 2010). CafA and CafB belong to the plant-type tetrameric β-CAs, whereas CafC and CafD are cab-type dimers. CafA and CafD are mitochondrial proteins, whereas CafB and CafC are cytoplasmic. CafA and CafB are constitutively and strongly expressed under ambient conditions, whereas CafC and CafD are weakly expressed under ambient conditions, but strongly activated by CO_2. Analysis of the effects of a series of gene deletion mutants demonstrated that only a ΔCafA ΔCafB double deletion mutant failed to grow under atmospheric CO_2 levels. Furthermore, CafA plays an

* Corresponding author.
E-mail address: misunjin@gist.ac.kr (M.S. Jin).

https://doi.org/10.1016/j.jsb.2021.107700
Received 19 November 2020; Received in revised form 22 January 2021; Accepted 23 January 2021
Available online 3 February 2021

important role in asexual differentiation, and only CafB can complement the function of β-CA Nce103 of *S. cerevisiae*. Collectively, these results indicate that CafA and CafB are the major β-CAs in *A. fumigatus,* whereas CafC and CafD are minor forms.

Recently we reported a biochemical and crystallographic characterization of CafA, which revealed the catalytic mechanism of CafA as well as pointing to a new class of antifungal compounds for treating invasive aspergillosis (Kim et al., 2020). In the present study, we describe a crystallographic analysis of CafB at 2.0–2.2 Å resolution. Surprisingly, we observed two remarkable novel zinc-free structures, as well as the classical zinc-bound structure, in the same space group. Combined with site-directed mutagenesis data, our findings lead to the following conclusions; (i) CafB uses a standard mechanism of enzyme activation dependent on strictly conserved catalytic residues. (ii) It is inactivated under low pH and/or oxidative stress when a zinc ion is expelled from the active site and a disulfide bond is formed between the two catalytic cysteines. (iii) It is also inactivated in zinc-depleted conditions by flipping the solvent-exposed zinc-ligating cysteine, making it incapable of binding substrate. (iv) It can also adopt typical active/inactive configurations in which a conserved aspartic acid functions as an on/off switch.

2. Materials and methods

2.1. Cloning, expression and purification

A codon-optimized gene encoding the full-length CafB (residues 1–228) of *A. fumigatus* was cloned into pET21a vector containing a hexahistidine tag followed by a thrombin protease site. Site-directed mutations were constructed by overlap polymerase chain reactions (PCR), and verified by sequencing. To overexpress proteins, recombinant plasmids were transformed into *Escherichia coli* BL21 (DE3) cells. The cells were grown at 37 °C in Lysogeny Broth medium supplemented with 0.1 mg/mL ampicillin. Protein expression was induced with 1 mM isopropyl-β-d-thiogalactopyranoside (IPTG) at an OD_{600} of approximately 0.6–0.7. Growth was continued at 20 °C for 16 h, and, after cell harvesting by centrifugation at 14,000 g for 15 min at 4 °C, the pellet was resuspended and lysed using a microfluidizer in a buffer containing 20 mM Tris-HCl pH 8.0, 200 mM NaCl, 20 mM imidazole, 10 μg/mL DNase I and 0.1 mM phenylmethylsulfonyl fluoride (PMSF). Cell debris and unbroken cells were removed by centrifugation at 31,000 g for 20 min, and the supernatant was loaded onto Ni-NTA affinity (Incospharm) resin. After washing with 10 column volumes of buffer, CafB protein was eluted with 20 mM Tris-HCl pH 8.0, 200 mM NaCl and a three-step gradient of imidazole, followed by removal of the hexahistidine tag with thrombin. The protein was further purified by HiTrap Q anion exchange chromatography (GE Healthcare) and Superdex 200 gel filtration chromatography (GE Healthcare) in a buffer containing 20 mM Tris-HCl pH 8.0 and 200 mM NaCl for the wild-type and 20 mM MES pH 6.0, 200 mM NaCl and 1 mM zinc chloride for the mutants. Fractions from the gel filtration column containing the protein were pooled and concentrated to 20 mg/ml for crystallization. All purification steps were performed at 4 °C.

2.2. Enzyme activity assays

In vitro CO_2 hydration assays followed the protocol described by Carter et al. with some modifications (Carter et al., 1969). Briefly, CO_2 solutions were freshly prepared by bubbling CO_2 gas into ice-chilled water for 1 h. CO_2-saturated water (4 mL) was then added to 6 mL of reaction buffer (20 mM Tris-HCl pH 8.5) to start the reaction in the presence or absence of purified enzyme (1 μM). Activity was monitored at 5 s intervals by measuring pH, which decreased from 8.3 to 6.3. Values presented are means of three replications using the same enzyme preparation.

2.3. Measuring thermal and pH stability

The thermal and pH stability of CafB was measured as previously described (Kim et al., 2020). Briefly, proteins (1 μM) were pretreated at temperatures from 22 °C to 100 °C for 15 min to measure thermal stability. To measure pH stability, 20 μL of protein (1 μM) was incubated at 4 °C for 4 h in 80 μL of 50 mM buffer at pH 4 and 7. Residual enzymatic activity was expressed as a percentage of the maximal activity at 22 °C and pH 7.

2.4. Crystallization, data collection and structure determination

Crystals of wild-type CafB were grown at 22 °C by the sitting-drop vapor diffusion method in two different conditions; (i) 0.1 M sodium acetate pH 4.0–4.5, 1.2–1.6 M ammonium sulfate (Crystal form I) and (ii) 0.1 M Tris-HCl pH 7.0–8.5, 28–30% (w/v) polyethylene glycol 2000 (PEG2000) and 0.1 M magnesium acetate (Crystal form II). Crystals of the Y159A mutant were obtained in 0.1 M sodium citrate pH 4–5 and 1.7–2.0 M sodium chloride supplemented with 10 mM Tris(2-carboxyethyl)phosphine hydrochloride (TCEP) (Crystal form III). The crystals appeared after 3–4 days and grew to full size within two weeks. They were cryoprotected in reservoir solution supplemented with 5–10% (v/v) ethylene glycerol or glycerol, and flash-frozen in liquid nitrogen. X-ray diffraction data were collected at beamlines 5C, 7A and 11C of the Pohang Accelerator Laboratory (PAL). The datasets were indexed, integrated and scaled with DENZO and SCALEPACK of the HKL2000 program package (Otwinowski and Minor, 1997). Initial phases were obtained by molecular replacement using the fungal β-CA CAS2 structure from *Sordaria macrospora* (PDB code 4O1K) as search probe (Lehneck et al., 2014; McCoy et al., 2007). A model was built manually according to the electron density map using COOT (Emsley and Cowtan, 2004). Multiple cycles of refinement were performed by REFMAC5 and PHENIX (Adams et al., 2010; Murshudov et al., 1997). The X-ray data collected and refinement statistics are listed in Supplementary Table 1. All figures were produced with PyMOL (http://www.pymol.org).

3. Results

3.1. Overall structure of CafB and its implications for thermal stability

In order to understand the catalytic mechanism of CafB, the full-length construct (26 kDa) was expressed in bacteria and purified to near homogeneity by anion exchange and size exclusion chromatography. The gel filtration profile showed that CafB was a stable tetrameric protein of 104 kDa in solution (Supplementary Fig. 1). The purified protein was crystallized and its high resolution structure determined by X-ray crystallography (Supplementary Table 1). Wild-type crystals were produced at two pHs, at acidic pH (form I) and at neutral or moderately basic pH (form II). Both condition yielded crystals belonging to the space group $P3_221$, where the first dimer is present in an asymmetric unit and the second is produced by the crystallographic 2-fold rotation axis, owing to the fact that the 2-fold symmetry axis is coincident with the crystallographic one (Fig. 1A and Supplementary Fig. 2). Superimposition analysis revealed that the monomers in the two crystal forms were very similar, with Cα rmsd below 0.5 Å, indicating that pH does not affect the overall fold of the protein (Figs. 1B and 2A).

The CafB crystal structure has the usual characteristics found in other plant-type β-CAs, including an N-terminal helix region, a central core comprising 10 α-helices and 5 β-strands (β2-β1-β3-β4-β5), and a C-terminal subdomain (Fig. 1B and Supplementary Fig. 3) (Cronk et al., 2006; Dostál et al., 2018; Lehneck et al., 2014; Schlicker et al., 2009). Although CafA and CafB have only 31% sequence identity, they share a similar overall fold with a Cα-rmsd of 2.0 Å, suggesting that the two closely related enzymes have similar catalytic mechanisms (Fig. 2A and Supplementary Fig. 3) (Kim et al., 2020). We observed that the N-

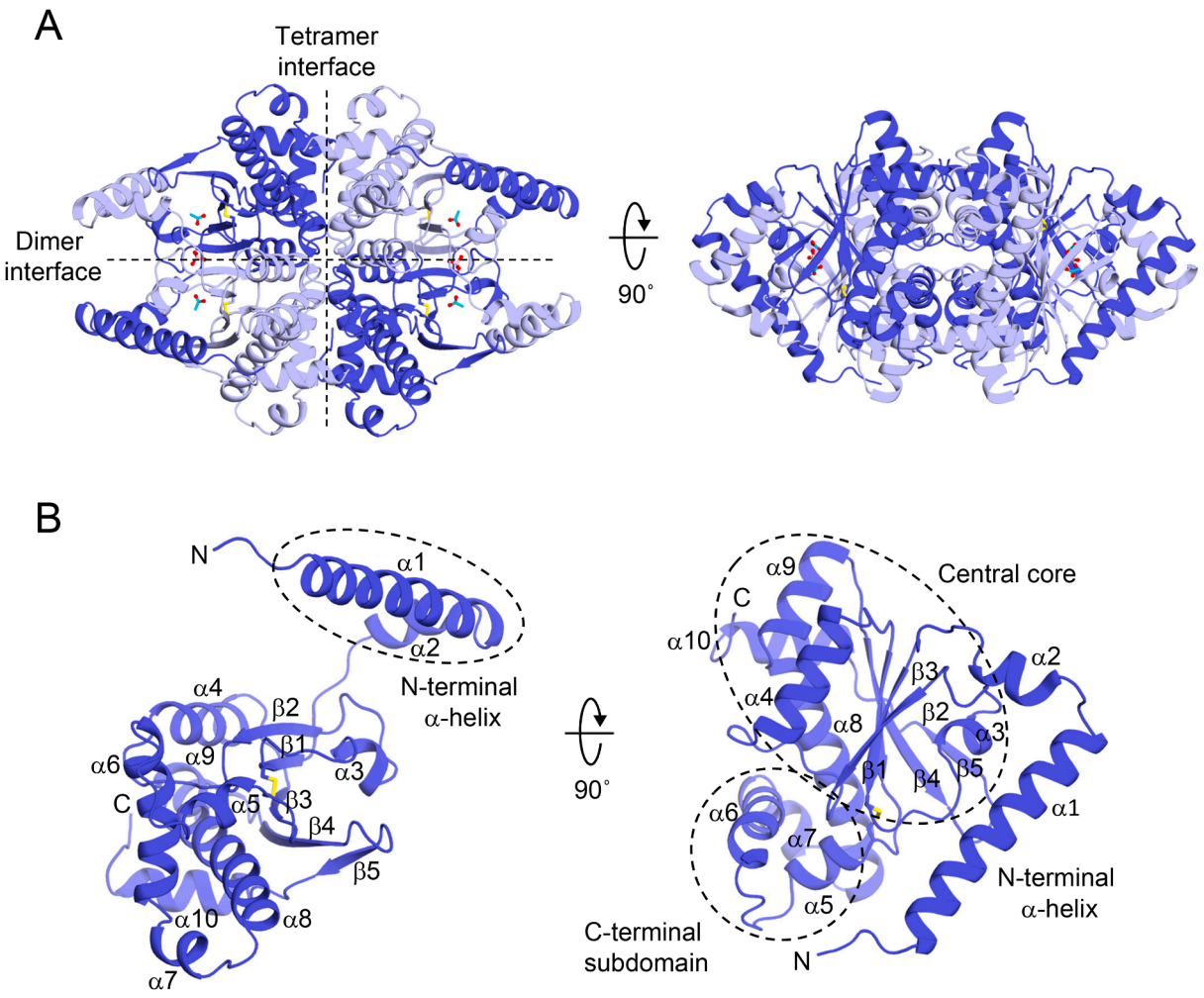

Fig. 1. The overall structure of CafB. (A) Cartoon representation of the CafB tetramer (form I). The tetramer is composed of two units of the dimer, which are related by a non-crystallographic 2-fold axis perpendicular to the plane of the paper. The disulfide bond at the active site is shown as a yellow stick model. Acetate and sulfate ions are shown as cyan and pink ball-and-stick models, respectively. Protein secondary structures were assigned using the STRIDE (Heinig and Frishman, 2004). (B) Structure of the CafB monomer. The subdomains within the monomer are indicated by black dashed circles.

terminal region of CafB contained 12 more residues than that of CafA. CafB activity was stable up to 80 °C, retaining more than 70% of its original activity (Fig. 2B). This high temperature stability is not entirely unexpected because *A. fumigatus* is capable of growing rapidly at 37 °C and tolerates temperatures above 50 °C, whereas most other fungi are mesophilic, with growth optima between 25 and 35 °C (Cooney and Emerson, 1964). By contrast, CafA loses most of its activity at temperatures above 50 °C (Kim et al., 2020). This greater thermal stability of CafB is most likely due to interfacial ionic and hydrophobic interactions between the longer N-terminal α-helix and the adjacent monomer (Fig. 2 and Supplementary Fig. 3).

3.2. The zinc-free and disulfide-bonded structure

Contrary to our expectation that the crystalline form of CafB would also have a typical active site in which the catalytic zinc ion is coordinated by a histidine and two cysteines, it in fact exists in two distinct inactive forms that have not been reported in any other CAs to date. In the crystal structure obtained at low pH (form I), a pair of catalytic cysteines (C57 and C116) form a disulfide bond with loss of the zinc ion and partial breakage of the highly conserved salt bridge between D59 and R61 (Fig. 3A). Comparison of the structures of CafA (zinc-bound active) and CafB (zinc-free inactive, form I) shows that in the latter a loop including C116 is shifted towards C57 by approximately 2 Å to form a stable disulfide bridge (Fig. 3A). Furthermore, the zinc-coordinating histidine (H113) is moved backwards as a result of an approximately 35° side chain rotation, thus escaping from the zinc-coordinating sphere and preventing steric clash with the disulfide bond. Previously, enzyme inactivation by disulfide bond formation has been reported in the cab-type dimeric β-CA, Rv1284, of *M. tuberculosis* (Nienaber et al., 2015). However, the disulfide bond in Rv1284 occurs between one of the zinc-coordinating cysteine residues (C35) and another cysteine residue (C61) in close proximity, generating a wider entrance to the active site (Fig. 3B).

There are three possible explanations for why a disulfide bond is formed between the active site cysteines in CafB. The first is that the disulfide bond is caused by oxidation of the zinc-coordinating cysteines during crystal growth, since we confirmed that the freshly purified enzyme was undoubtedly active (Fig. 3C). This assumption is supported by the fact that the enzyme incubated for 10 min with 5 mM H_2O_2 (a relatively mild oxidant) had significantly reduced activity, but that activity was partially restored by incubation in the presence of the reducing agent TCEP and zinc chloride (Fig. 3C). This reversible redox-dependent regulation, in which zinc/cysteine-based enzymes lose catalytic activity when a disulfide bond is formed and oxidative release of the catalytic zinc ion occurs, is frequently observed in nature (Evans et al., 2002; Klomsiri et al., 2011; Pace and Weerapana, 2014; Paulsen and Carroll, 2010; Shaban et al., 2016). The second possibility is that the

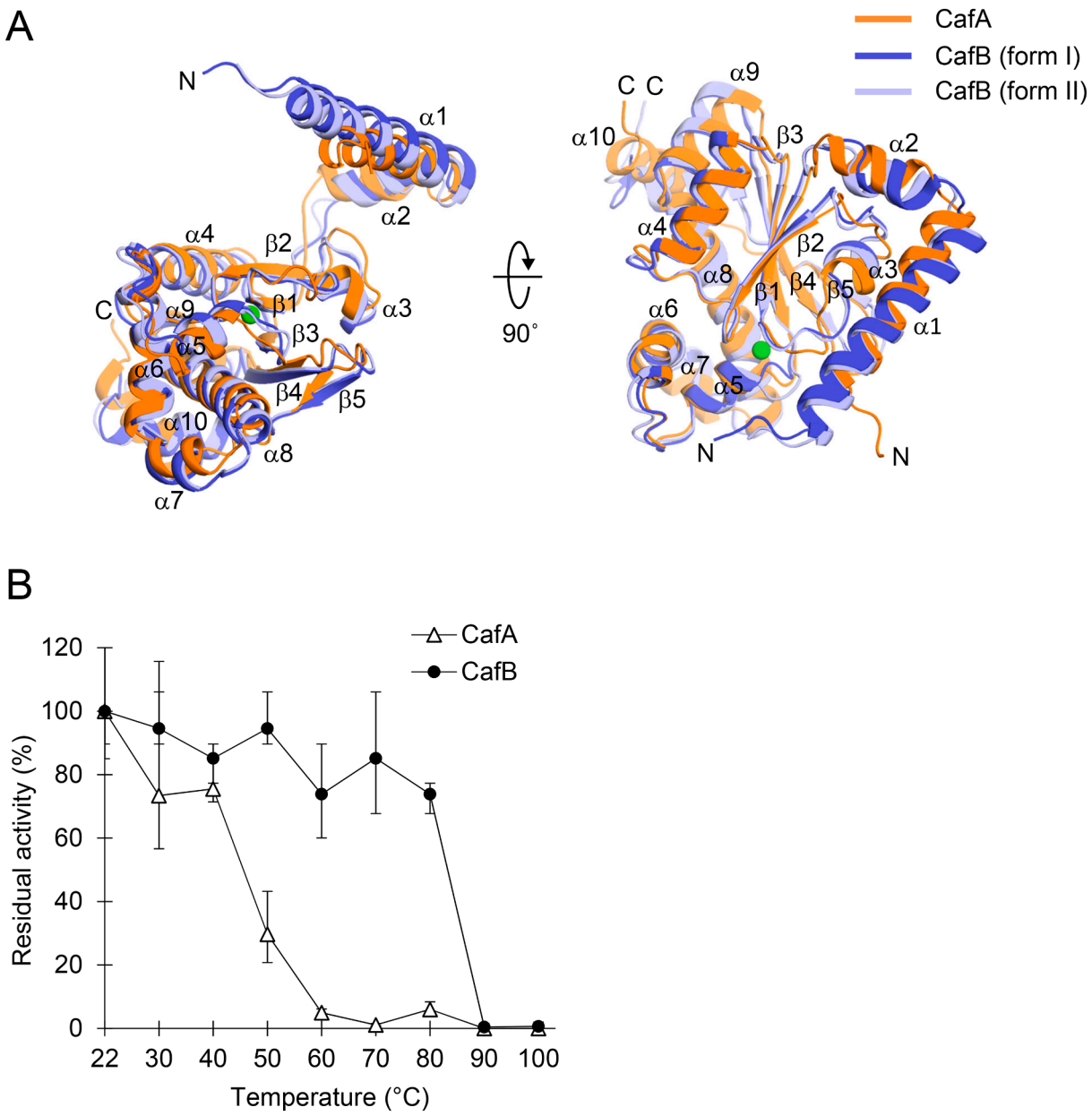

Fig. 2. Comparison of the structures and thermal stabilities of CafA and CafB. (A) The monomers of CafA (PDB ID 7COI) and CafB (form I and II) are aligned. The zinc ion of CafA is shown as a green sphere. (B) Thermal stability of the purified CafA and CafB. Maximum activities at 22 °C were set at 100%. Thermal stability of CafA was measured in a previous study (Kim et al., 2020). Each point is the mean of three separate replicate experiments using the same protein preparation. Error bars represent SDs (±standard deviations).

low pH of the crystallization solution causes a significant change in the metal coordination environment. At low pH the catalytic histidine (pKa of 6.0) and cysteine (pKa of 8.3) residues are likely to be protonated, which might distort the metal coordination and facilitate release of the zinc ion. Subsequent formation of the disulfide bridge may play a key role in stabilizing the zinc-free structure. This idea is consistent with data showing that when CafB is exposed to pH 4 buffer, *in vitro* CO_2 hydration activity decreases to one fifth of its original activity at pH 7 (Fig. 3D). The third possibility is that the crystallization conditions mimic a zinc-depleted environment, as zinc ions are not added to the crystallization and cryoprotectant solutions. We also considered the possibility that the high concentration of anionic salts (i.e. acetate or sulfate) in the crystallization solution might chelate zinc. However, this idea is excluded by the fact that when the enzyme is incubated with such anions for 24 h it retained almost all of its enzyme activity (data not shown).

3.3. Modulation of CafB activity by flipping a solvent-exposed catalytic cysteine

The CafB crystal obtained under neutral or moderately alkaline conditions (form II) was also novel for the inactive form of an enzyme where the conserved active site residues have a unique conformation. Structural comparison of CafA (zinc-bound active) and CafB (zinc-free inactive, form II) revealed that, in the latter, a solvent-exposed catalytic cysteine (C116) has undergone a 180° flip (Fig. 4A and Supplementary Fig. 4). In addition, H113 is rotated by ~36 degrees and D59 and R61 form a partially broken salt bridge. The net result of these changes is that the tetrahedral geometry is destroyed and the zinc ion removed. The flipping of C116 also contributes to widening the active site entrance by increasing the distance between the two catalytic cysteines from 8 Å to 10.8 Å (Fig. 4B). As a result, the active site is easily accessed by water molecules (W1-3). Of these water molecules, W1 and W2 are tightly

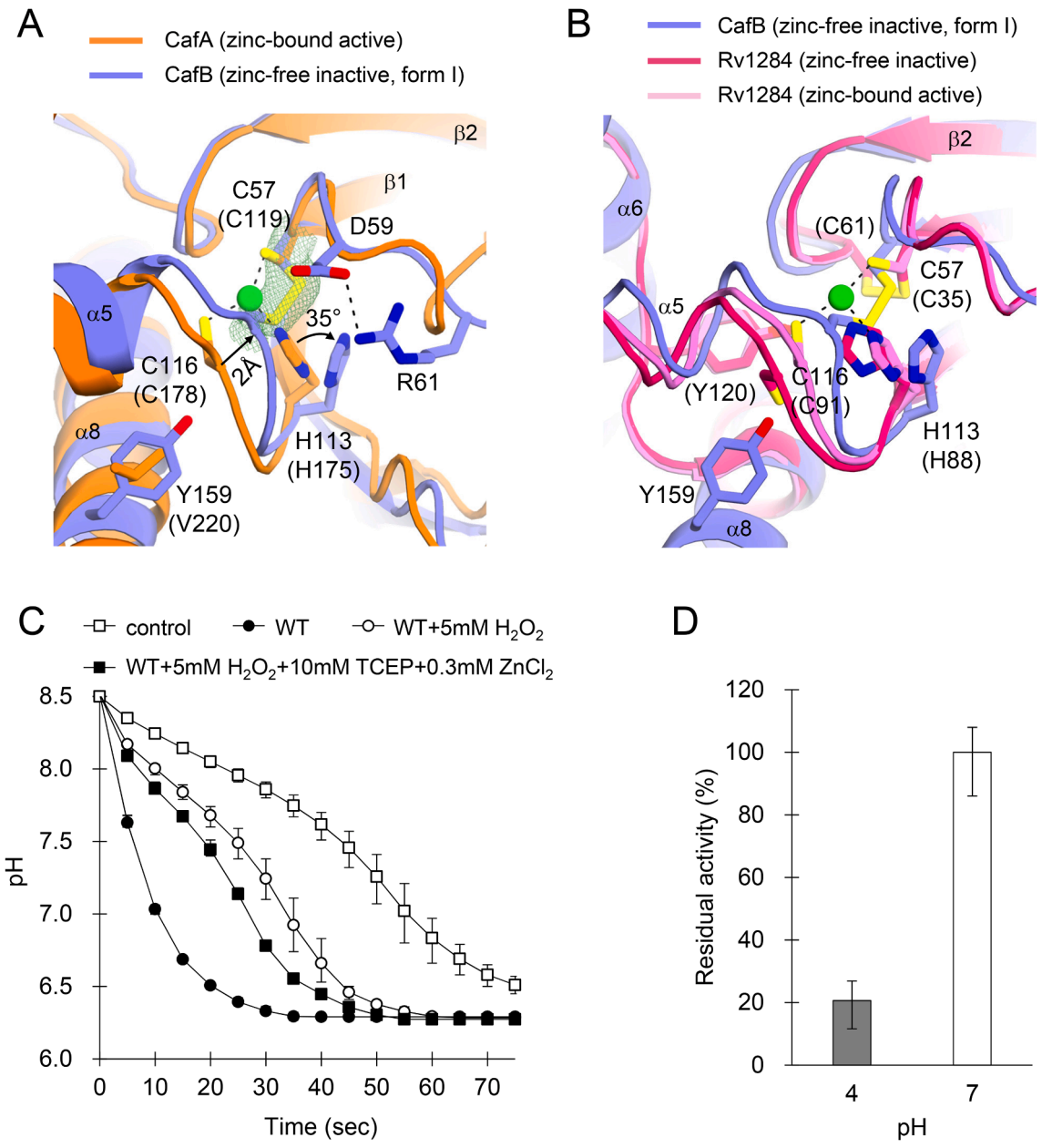

Fig. 3. Formation of the zinc-free disulfide bond. (A) Comparison of the structures of the active sites of CafA (PDB ID 7COI) and CafB (form I). Key residues in the active sites are shown in stick representation. The Fo-Fc map superimposed on the disulfide bond is contoured at 2.5 σ level. The zinc ion present in CafA is shown as a green sphere. Structural changes are marked by black arrows. Amino acids in parentheses represent substitutions found in CafA. (B) Comparison of the structures of the active sites of CafB (form I), Rv1284 (PDB IDs 4YF5 (inactive form) and 4YF4 (active form)). Residues in parentheses represent the substitutions found in Rv1284. (C) CO_2 hydration activity of CafB in various conditions. Data are means (±standard deviations, SDs) of three independent experiments. Error bars indicate SDs. (D) pH stability of purified CafB. CO_2 hydration activity at pH 7.0 is set at 100%.

bound around C57, and W2 and W3 act as a bridge giving rise to a hydrogen bond network between C57 and the backbone nitrogens of G118 and V119. These findings demonstrate that CafB can be stabilized even though the catalytic zinc and disulfide bond are absent from the active site.

To understand how C116 can be easily flipped, we focused on the two glycine residues (G117 and G118) next to C116 (Supplementary Fig. 3). In the final model, with a higher than average B factor in the protein (73 $Å^2$ vs 51 $Å^2$), the electron density map for G117 was not visible or very weak, indicating that this residue has high structural flexibility allowing rapid structural rearrangement in response to the presence or absence of zinc ions (Supplementary Fig. 4). This suggests that when CafB is exposed to limiting zinc conditions for a long time (as in our crystallization conditions), there is no zinc in the active site but structural integrity is maintained either by disulfide bond formation (Fig. 3A) or by a water-mediated hydrogen bond network in the active site (Fig. 4B). Thus, zinc is essential for regulating enzyme activity, not for structural integrity.

3.4. The structure of zinc-bound CafB

In order to generate zinc-bound crystals, we originally tested (i) purification and crystallization of wild-type CafB in the presence of reducing agent and zinc chloride, (ii) bubbling nitrogen gas into buffer to remove the dissolved O_2, and (iii) co-crystallization with the CA inhibitor acetazolamide. However, all these approaches were unsuccessful

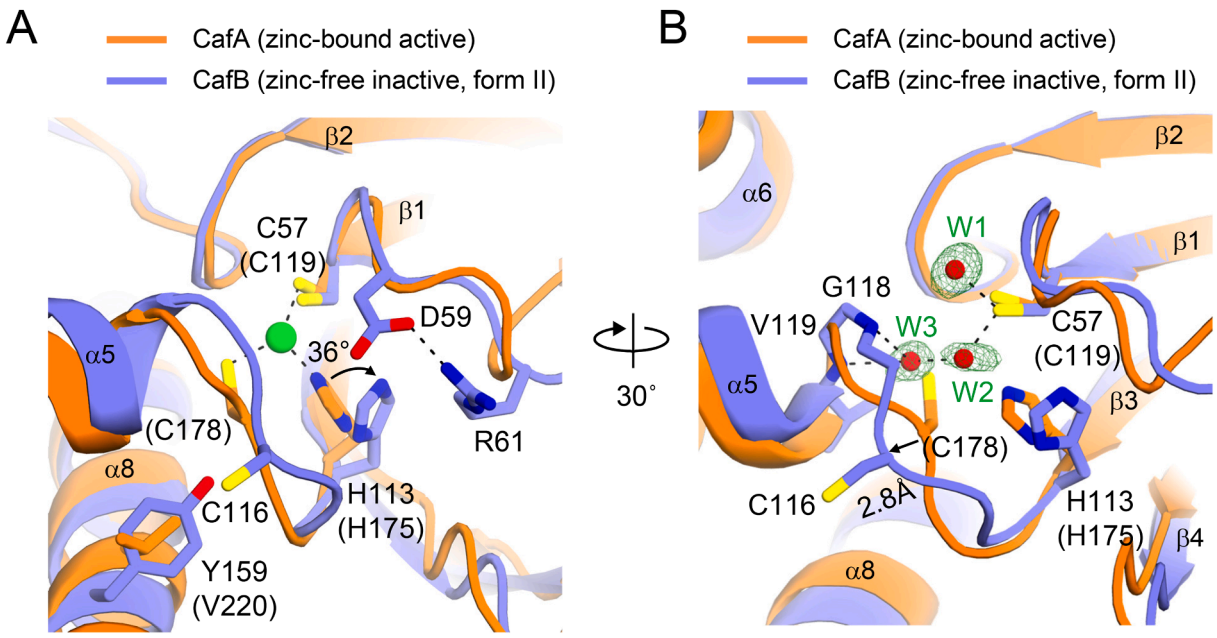

Fig. 4. Inactivation of CafB by C116 flipping. (A) Structure comparison of the active sites of CafA (PDB ID 7COI) and CafB (form II). The zinc ion present in CafA is shown as a green sphere. Amino acids in parentheses represent substitutions found in CafA. Structural changes are marked by black arrows. (B) The water molecules in CafB are shown as red spheres. The Fo-Fc map superimposed on the refined water molecules (W1, W2 and W3) are contoured at 4, 3.8 and 3 σ level, respectively. The zinc ion in CafA, as well as the D59-R61 pair and Y159 residue in CafB, are omitted for clarity.

(data not shown). Eventually we noted the presence of the solvent-exposed Y159, which is located right behind C116 (Fig. 3A). It has been shown that weakly hydrophilic and aromatic amino acids, particularly tyrosines, are frequently found around disulfide bonds, suggesting that they may mediate proton shuttling during disulfide oxidation (Marques et al., 2010). Inspection of the CafB and Rv1284 structures indicated that both enzymes had solvent-exposed tyrosine residues (Y159 in CafB and Y120 in Rv1284), approximately 5 Å from the disulfide bond, although at different positions within the protein (Supplementary Fig. 5A and C) and so might play this role in oxidative inactivation of the corresponding enzymes (Nienaber et al., 2015). In contrast, in most other β-CAs aliphatic and hydrophobic amino acids, such as alanine, leucine, isoleucine and valine, occupy the equivalent locations, although in CAS2 of *S. macrospora* there is also a tyrosine (Y158) (Supplementary Fig. 5C) (Cronk et al., 2006; Dostál et al., 2018; Kim et al., 2020; Kimber and Pai, 2000; Lehneck et al., 2014; McGurn et al., 2016; Nienaber et al., 2015; Schlicker et al., 2009; Teng et al., 2009). To confirm the proposed role of Y159 as electron carrier, we performed site-directed mutagenesis, changing Y159 to alanine or valine (Y159A or Y159V). Although the wild-type and Y159V mutant had similar levels of expression and activities (Fig. 5A), the wild-type enzyme had little catalytic activity after storage for two weeks at 4 °C, whereas the Y159V mutant retained significant activity. Evidently, therefore, Y159 mediates the electron flow for catalytic disulfide bond

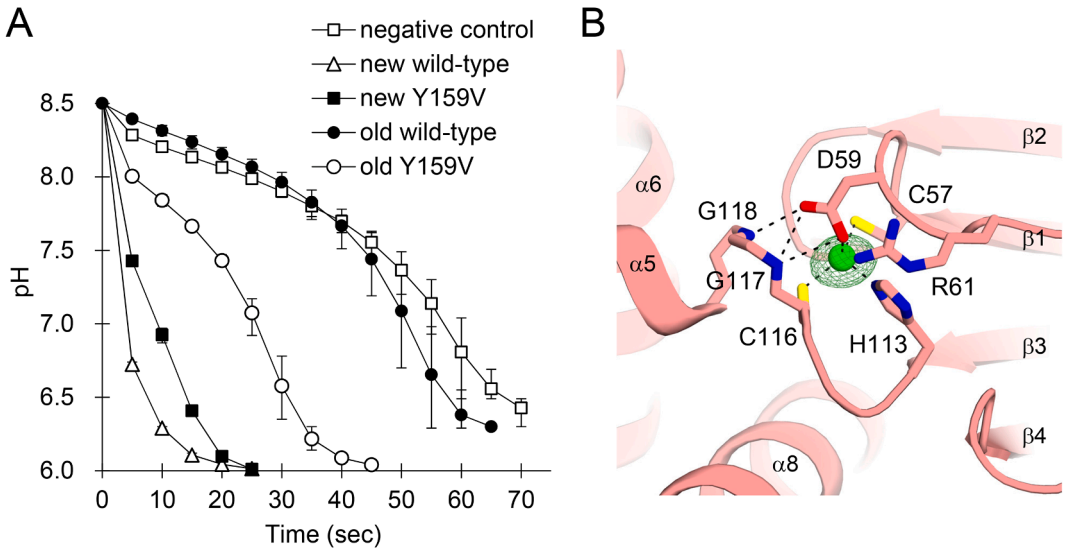

Fig. 5. The oxidative stress-resistant mutant and its active site structure. (A) CO_2 hydration activities of CafB variants. Data are means (±standard deviations, SDs) of three independent experiments. Error bars indicate SDs. (B) Close-up view of the zinc-coordinating sphere in the Y159A mutant (form III). The structure of the mutant is drawn in salmon to differentiate it from the wild-type. Key residues in the active site are shown in stick representation. The zinc ion is shown as a green sphere. The Fo-Fc map superimposed on the refined zinc ion is contoured at 8 σ level.

formation and renders cafB more sensitive to oxidative stress than other β-CAs.

The structure of the Y159A mutant was determined in the presence of reducing agent and zinc chloride. Like wild-type CafB, the dimeric form of the Y159A mutant (form III) was present in the asymmetric unit and the second dimer was produced by a crystallographic 2-fold rotation axis. Structure comparison of the wild-type and Y159A mutant indicated that despite the overall similarities of structure, there were notable differences at their active sites. The Y159A mutant had a catalytic zinc ion at the expected position (Fig. 5B) and all the zinc coordination sites were fully occupied by amino acids (C57, H113, C116 and D59) that replaced the zinc-bound water, thus forming a Type-II or closed conformation. At the same time the bond between D59 and R61 was completely disrupted, and the conformation of D59 stabilized by hydrogen bonds and ionic interactions with the backbone nitrogens of G117 and G118 (Fig. 5B).

3.5. Structural similarities between CafB and allosteric bacterial β-CAs

Interestingly, the CafB structure bears a strong resemblance to the

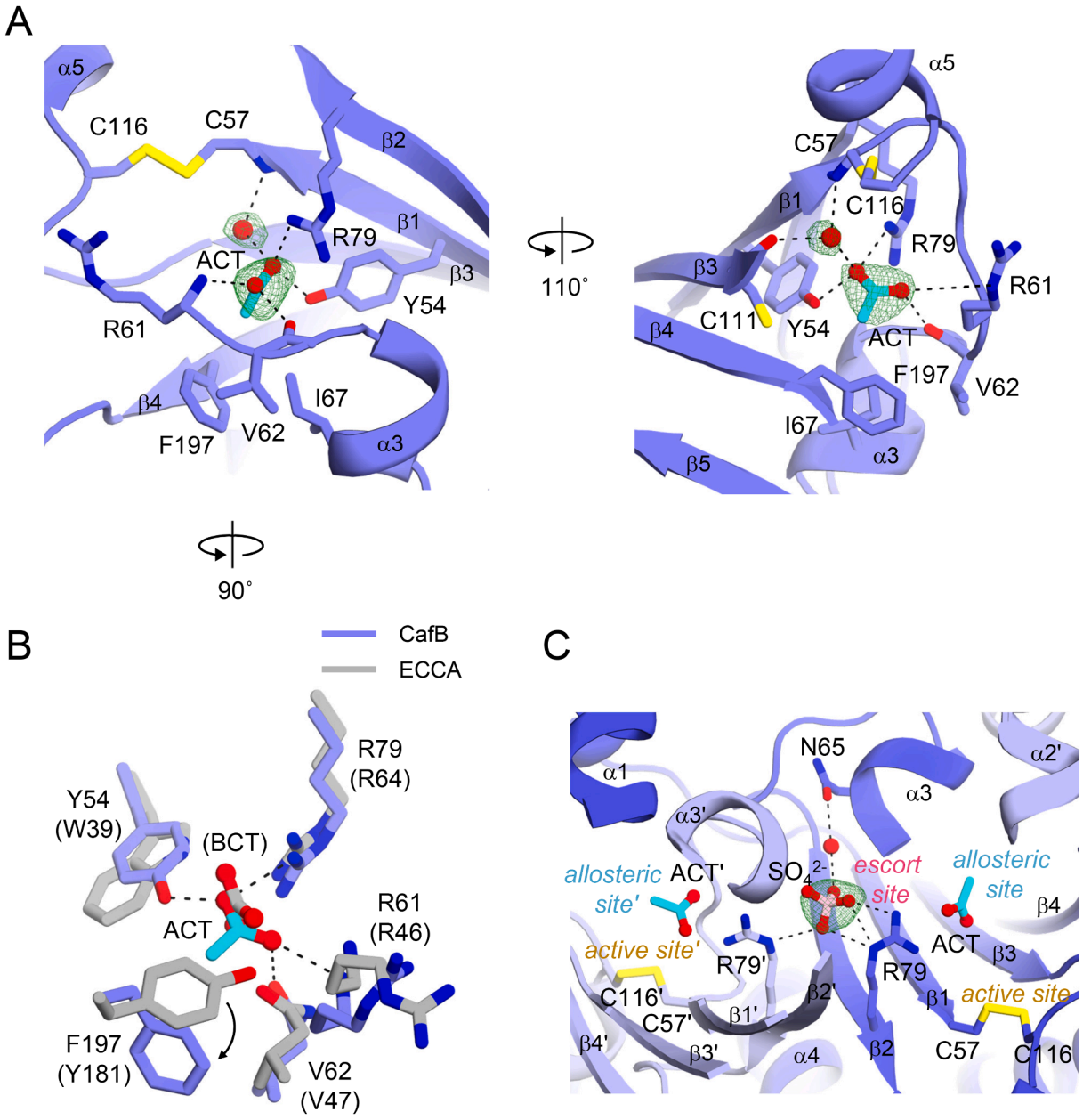

Fig. 6. Structural similarities between CafB and allosteric bacterial β-CAs. (A) Key residues at the presumed non-catalytic binding site (form I) are shown as stick models. The bound acetate (ACT) is represented as a ball-and-stick model. The water molecule is shown as a red sphere. The hydrogen bonds and ionic interactions are shown by dashed lines. The Fo-Fc maps superimposed on the refined ACT and on a water molecule are contoured at 3σ level, respectively. The catalytic disulfide bond in the vicinity is also shown. (B) Comparison of the structures of the non-catalytic binding sites of CafB and ECCA (PDB ID 2ESF). The side chains of residues that coordinate ACT and bicarbonate (BCT) in CafB and ECCA, respectively, are shown in stick representation. The substantial structural difference is marked by a black arrow. Amino acids in parentheses represent the corresponding residues in ECCA. (C) The sulfate ion (SO_4^{2-}) trapped at the dimerization interface (escort site) of CafB (form I). The sulfate ion is shown as a pink ball-and-stick model. The Fo-Fc map superimposed on the sulfate ion is contoured at the 3.5 σ level. The nearby acetate ions and disulfide bonds are also shown. Single apostrophes are used for all the residues of one monomer to differentiate them from those of the other monomer.

previously determined structures of allosteric bacterial β-CAs, suggesting that they are probably evolutionarily related. We found that wild-type CafB (forms I and II) contains an adventitious acetate molecule (Fig. 6A), presumably originating from the crystallization solution, in a position similar to that of the bicarbonate responsible for allosteric regulation in β-CAs of *E. coli* (ECCA, PDB ID 2ESF) and *H. influenza* (HICA, PDB ID 2A8D) (Cronk et al., 2006). In ECCA (and HICA), the bicarbonate binding site is located approximately 8 Å from the disulfide bond, and the bicarbonate is firmly anchored by multiple hydrogen bonds with W39, R64 and Y181 and the backbone oxygen of V47 (Fig. 6B). Similarly, in CafB the carboxylate group of acetate interacts with Y54, R79, and the backbone oxygen and nitrogen of V62 and R61, respectively (Fig. 6A). On the other hand, the methyl group of acetate is surrounded by the hydrophobic residues I67 and F197, making van der

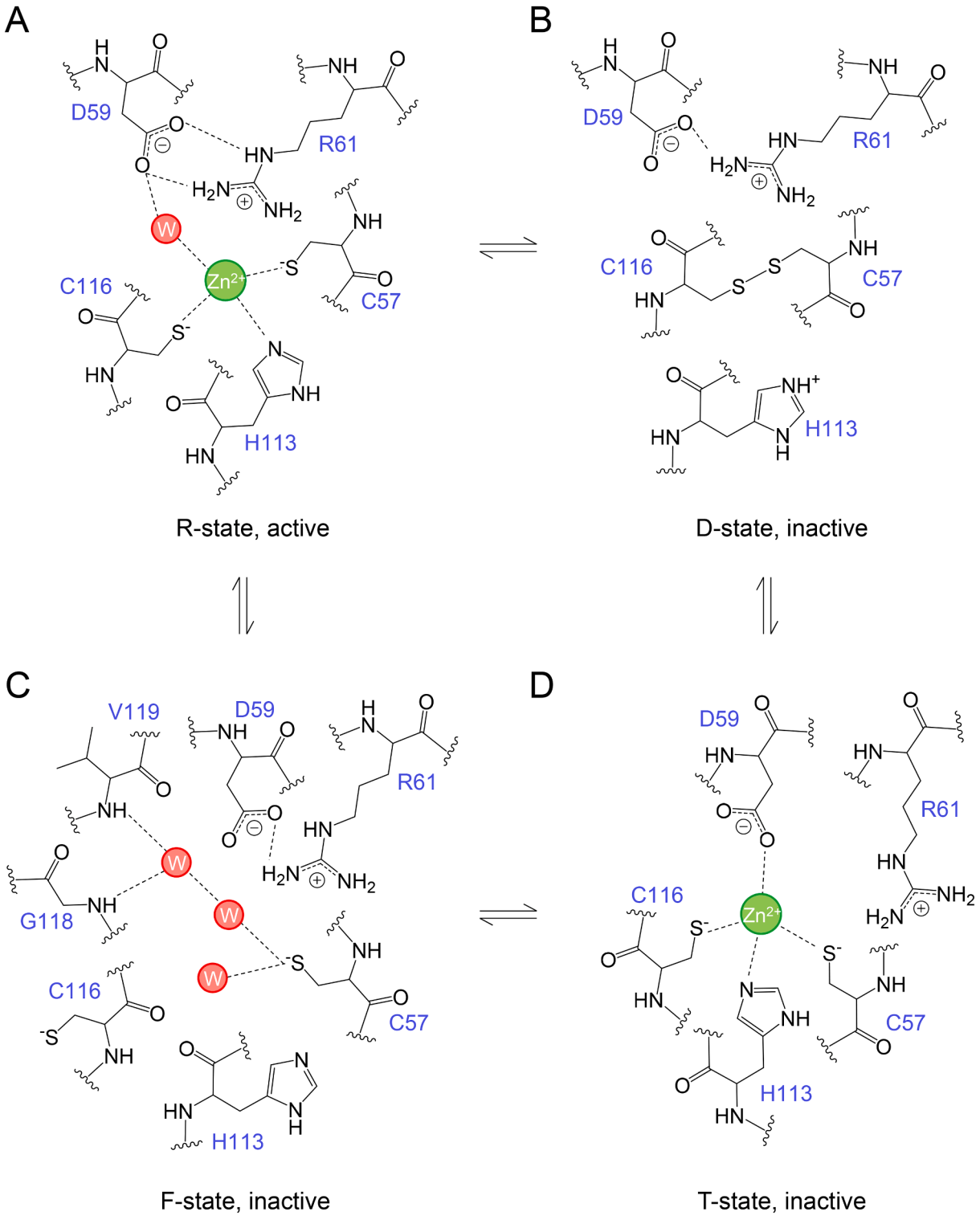

Fig. 7. A possible mechanism of regulation of CafB activity. (A) The proposed zinc-bound active conformation (R-state). (B and C) The zinc-free and inactive conformations resulting from (B) disulfide bond formation between the catalytic cysteines C57 and C116 (D-state) or (C) flipping of catalytic C116 (F-state). (D) The zinc-bound inactive conformation (T-state). Figures (A) and (D) are modified from (Cronk et al., 2006).

Waals interactions. Structure comparison revealed that the acetate bound to CafB is ~1.3 Å closer to F197, and occupies some of the space created by rotation of the phenyl ring (Fig. 6B). This seems to create room for the larger CH_3 group of acetate and avoid any collision with F197. In our structure the acetate also forms hydrogen bonds via a single buried water molecule, to the backbone nitrogen and oxygen of C57 and C111, respectively (Fig. 6A). A highly ordered water molecule, with a 42 $Å^2$ of B factor value, is often found in the β-CA family, and the coordinating residues are highly conserved (Cronk et al., 2006; Kimber and Pai, 2000; Mitsuhashi et al., 2000).

A sulfate ion (form I) derived from the crystallization solution is present in the dimerization interface, and known as an escort site (Fig. 1A and 6C) (Hoffmann et al., 2015; Rowlett et al., 2010). The sulfate binding site is located approximately 8 Å from an acetate in a non-catalytic binding site, and the sulfate is bound by multiple salt bridges between the neighboring R79 and a water-mediated hydrogen bond with N65. This situation is highly reminiscent of previous HICA data showing that three mutants (G41A, V47A and W39V/G41A) adopt a closed active site structure (i.e. an aspartic acid replaces the zinc-bound water molecule) with an inhibitory bicarbonate (or sulfate) ion in the escort site (Hoffmann et al., 2015; Rowlett et al., 2010). This similar binding mode suggests that the escort site of CafB may also function as an intermediate binding site along the bicarbonate entry and exit pathway because it is open to the bulk solvent and continuous with the presumed non-catalytic bicarbonate binding site (Chovancova et al., 2012).

4. Discussion

We have determined the crystal structures of CafB with and without the zinc ion. Our results, together with previous data for CafA, allow us to propose possible mechanisms that regulate the activities of the major β-CAs in *A. fumigatus* (Fig. 7). The catalytic sites of CafA and CafB closely resemble those of other β-CAs (Huang et al., 2011; Lehneck et al., 2014; Mitsuhashi et al., 2000; Strop et al., 2001). Specifically, the two cysteines and a histidine responsible for the coordination of zinc are conserved (Fig. 7A and Supplementary Fig. 5C) (Fukasawa et al., 2015). The D-R pair regulating CO_2 access to the active site is also conserved. These findings strongly suggest that both enzymes employ a catalytic mechanism, involving substrate binding, proton transfer, and product release (R-state) common to other β-CAs (Cronk et al., 2006).

The data obtained in this study reveal that inactivation of CafB can be achieved by disrupting coordination of the zinc ion followed by stripping of the ion from the active site. The zinc-free structures obtained display the active sites in two conformations; (i) One has a catalytic disulfide bond that maintains structural integrity (D-state, Fig. 3A and 7B). This form was primarily observed after crystallization at pH 4.0–5.5. Therefore, we imagine that CafB undergoes oxidative inactivation in acidic conditions (Nienaber et al., 2015). Proton shuttling residues in CAs, such as H64 of human α-CA II, H216 of the β-CA from *Arabidopsis thaliana* and E84 of the γ-CA from *Methanosarcina thermophile*, are commonly found in dual conformations of the side chains, one of which points toward the active site ("in" position) the other to the solvent ("out" position) (Fisher et al., 2007; Maupin and Voth, 2007; Mikulski and Silverman, 2010; Rowlett et al., 2002; Tripp and Ferry, 2000). The structure of Y158 of *S. macrospora* CAS2 (corresponding to Y159 in CafB) has also been found in two distinct orientations (Supplementary Fig. 5B), suggesting that the tyrosine residues in the vicinity of the catalytic cysteines play a role in electron movement during disulfide bond formation (Lehneck et al., 2014). (ii) The other form has a unique conformation in which the solvent-exposed catalytic cysteine (C116) is highly flexible due to the absence of the zinc ion and can flip to an outward orientation (F-state, Fig. 4). We propose that structural water molecules within the active site compensate for the absence of zinc by forming unique water-cysteine interactions (Fig. 4B and 7C). Alternatively, the conserved aspartic acid residue (D59), which is conformationally mobile, may act as an on/off switch by forming a D-R pair and regulating enzyme activity (T-state, Fig. 5B and 7D) (Cronk et al., 2006).

Aspergillus fumigatus is a saprophytic fungus responsible for the decomposition of organic material in the soil, and plays an essential role in the carbon and nitrogen cycle (Latgé, 1999; Mullins et al., 1976). It is also the primary causative agent of invasive pulmonary aspergillosis (Pfaller and Diekema, 2010; Steinbach et al., 2012). When infecting humans, it needs to be resistant to the substantial change in CO_2 level from the atmospheric concentration (0.033%) to that of the host (5%). Therefore, CO_2 sensing and metabolism through CafA-D may play a pivotal role in its growth, survival and pathogenicity. It has been previously reported that deletion of the *nce103* gene encoding a plant-like β-CA in *S. cerevisiae* causes a high CO_2-requiring (HCR) phenotype and inability to grow in ambient air (Amoroso et al., 2005; Götz et al., 1999), while elevated Nce103 expression is observed in low CO_2 concentrations. Other fungal pathogens, namely *C. glabrata*, *C. albicans* and *C. neoformans,* have also been shown to display the HCR phenotype as a result of β-CA deletion (Bahn et al., 2005; Klengel et al., 2005; Mogensen et al., 2006). This suggests that a functional β-CA is required for fungal species to grow in their natural habitat, and that its inactivation is an absolute requirement for pH homeostasis when CO_2 levels are high. In this connection, *A. fumigatus* seems to have evolved specialized mechanisms of tolerance to high CO_2 during human infection. Therefore, it is likely that zinc-free CafB mimics the HCR phenotype of *A. fumigatus,* enhancing its survival in infected humans.

The binding of acetate by the CafB structure is the first example of non-catalytic substrate binding in fungi (Fig. 6A). The strong similarity between the binding modes of CafB and ECCA suggests that similar mechanisms underlie allosteric regulation by substrate in fungal and bacterial β-CAs, although the precise mechanisms and physiological role of such allosteric regulation is not clear. Despite a very high level of structural similarity, we recognize that current data alone are not sufficient to determine whether CafB is indeed allosterically regulated or whether acetate binding at a presumed non-catalytic binding site is coincidently coupled to the disorder state of the active site caused by loss of the zinc ion. To clearly address this question, we are currently investigating the kinetics and pH-dependent cooperativity of CafB.

CRediT authorship contribution statement

Subin Kim: Conceptualization, Methodology, Validation, Formal analysis, Investigation, Data curation, Writing - original draft, Visualization. **Jungyoon Yeon:** Methodology, Formal analysis, Investigation, Data curation, Visualization. **Jongmin Sung:** Methodology, Investigation. **Na Jin Kim:** Methodology, Investigation, Data curation. **Semi Hong:** Methodology, Investigation, Data curation. **Mi Sun Jin:** Conceptualization, Writing - review & editing, Supervision, Funding acquisition.

Declaration of Competing Interest

The authors declare that they have no known competing financial interests or personal relationships that could have appeared to influence the work reported in this paper.

Acknowledgements

We thank the beamline staff at the Pohang Accelerator Laboratory (PAL) for help with data collection and processing. We also would like to thank Dr. Julian Gross for critical reading of the manuscript. This work was supported by a grant from the National Research Foundation (NRF), funded by the Ministry of Science, ICT, and Future Planning of Korea (grant number: NRF-2017M3A9F6029753 and NRF-2019M3E5D6063908) and from the GIST Research Institute (GRI) IIBR funded by the GIST in 2020.

Accession codes

Coordinates and structure factors for CafB have been deposited in the Protein Data Bank under accession codes 7CXX (zinc-free and disulfide-bonded, crystal form I), 7CXW (zinc-free and a catalytic cysteine flipped, crystal form II), and 7CXY (zinc-bound inactive, crystal form III).

Author contributions

All the authors designed and performed experiments, discussed the results and contributed to the final manuscript. S.K., J.Y. and J.S. purified and crystallized the protein. S.K. determined the crystal structures. S.K., J.Y., N.J.K. and S.H. performed the enzyme activity tests. S.K. and J.Y. prepared the figures. S.K. and M.S.J. wrote the manuscript.

Appendix A. Supplementary data

Supplementary data to this article can be found online at https://doi.org/10.1016/j.jsb.2021.107700.

References

Adams, P.D., Afonine, P.V., Bunkóczi, G., Chen, V.B., Davis, I.W., Echols, N., Headd, J.J., Hung, L.W., Kapral, G.J., Grosse-Kunstleve, R.W., McCoy, A.J., Moriarty, N.W., Oeffner, R., Read, R.J., Richardson, D.C., Richardson, J.S., Terwilliger, T.C., Zwart, P.H., 2010. PHENIX: a comprehensive Python-based system for macromolecular structure solution. Acta Crystallogr. D Biol. Crystallogr. 66, 213–221.

Amoroso, G., Morell-Avrahov, L., Müller, D., Klug, K., Sültemeyer, D., 2005. The gene NCE103 (YNL036w) from *Saccharomyces cerevisiae* encodes a functional carbonic anhydrase and its transcription is regulated by the concentration of inorganic carbon in the medium. Mol. Microbiol. 56, 549–558.

Bahn, Y.S., Cox, G.M., Perfect, J.R., Heitman, J., 2005. Carbonic anhydrase and CO_2 sensing during *Cryptococcus neoformans* growth, differentiation, and virulence. Curr. Biol. 15, 2013–2020.

Carter, J.M., Havard, D.J., Parsons, D.S., 1969. Electrometric assay of rate of hydration of CO_2 for investigation of kinetics of carbonic anhydrase. J. Physiol. 204, 60P–62P.

Chovancova, E., Pavelka, A., Benes, P., Strnad, O., Brezovsky, J., Kozlikova, B., Gora, A., Sustr, V., Klvana, M., Medek, P., Biedermannova, L., Sochor, J., Damborsky, J., 2012. CAVER 3.0: a tool for the analysis of transport pathways in dynamic protein structures. PLoS Comput. Biol. 8, e1002708.

Covarrubias, A.S., Bergfors, T., Jones, T.A., Högbom, M., 2006. Structural mechanics of the pH-dependent activity of beta-carbonic anhydrase from *Mycobacterium tuberculosis*. J. Biol. Chem. 281, 4993–4999.

Cronk, J.D., Rowlett, R.S., Zhang, K.Y., Tu, C., Endrizzi, J.A., Lee, J., Gareiss, P.C., Preiss, J.R., 2006. Identification of a novel noncatalytic bicarbonate binding site in eubacterial beta-carbonic anhydrase. Biochemistry 45, 4351–4361.

Cooney, D.G., Emerson, R., 1964. Thermophilic fungi. An account of their biology, activities and classification.

Del Prete, S., Vullo, D., Scozzafava, A., Capasso, C., Supuran, C.T., 2014a. Cloning, characterization and anion inhibition study of the delta-class carbonic anhydrase (TweCA) from the marine diatom *Thalassiosira weissflogii*. Bioorg. Med. Chem. 22, 531–537.

Del Prete, S., Vullo, D., Fisher, G.M., Andrews, K.T., Poulsen, S.A., Capasso, C., Supuran, C.T., 2014b. Discovery of a new family of carbonic anhydrases in the malaria pathogen *Plasmodium falciparum*–the eta-carbonic anhydrases. Bioorg. Med. Chem. Lett. 24, 4389–4396.

Dostál, J., Brynda, J., Blaha, J., Macháček, S., Heidingsfeld, O., Pichová, I., 2018. Crystal structure of carbonic anhydrase CaNce103p from the pathogenic yeast *Candida albicans*. BMC Struct. Biol. 18, 14.

Elleuche, S., Pöggeler, S., 2009. Evolution of carbonic anhydrases in fungi. Curr. Genet. 55, 211–222.

Emsley, P., Cowtan, K., 2004. Coot: model-building tools for molecular graphics. Acta Crystallogr. D Biol. Crystallogr. 60, 2126–2132.

Evans, J.C., Huddler, D.P., Jiracek, J., Castro, C., Millian, N.S., Garrow, T.A., Ludwig, M. L., 2002. Betaine-homocysteine methyltransferase: zinc in a distorted barrel. Structure 10, 1159–1171.

Ferraroni, M., Del Prete, S., Vullo, D., Capasso, C., Supuran, C.T., 2015. Crystal structure and kinetic studies of a tetrameric type II beta-carbonic anhydrase from the pathogenic bacterium *Vibrio cholerae*. Acta Crystallogr. D Biol. Crystallogr. 71, 2449–2456.

Fisher, S.Z., Maupin, C.M., Budayova-Spano, M., Govindasamy, L., Tu, C., Agbandje-McKenna, M., Silverman, D.N., Voth, G.A., McKenna, R., 2007. Atomic crystal and molecular dynamics simulation structures of human carbonic anhydrase II: insights into the proton transfer mechanism. Biochemistry 46, 2930–2937.

Fukasawa, Y., Tsuji, J., Fu, S.C., Tomii, K., Horton, P., Imai, K., 2015. MitoFates: improved prediction of mitochondrial targeting sequences and their cleavage sites. Mol. Cell. Proteomics 14, 1113–1126.

Götz, R., Gnann, A., Zimmermann, F.K., 1999. Deletion of the carbonic anhydrase-like gene NCE103 of the yeast *Saccharomyces cerevisiae* causes an oxygen-sensitive growth defect. Yeast 15, 855–864.

Han, K.H., Chun, Y.H., Figueiredo Bde, C., Soriani, F.M., Savoldi, M., Almeida, A., Rodrigues, F., Cairns, C.T., Bignell, E., Tobal, J.M., Goldman, M.H., Kim, J.H., Bahn, Y.S., Goldman, G.H., Ferreira, M.E., 2010. The conserved and divergent roles of carbonic anhydrases in the filamentous fungi *Aspergillus fumigatus* and *Aspergillus nidulans*. Mol. Microbiol. 75, 1372–1388.

Heinig, M., Frishman, D., 2004. STRIDE: a web server for secondary structure assignment from known atomic coordinates of proteins. Nucleic Acids Res. 32, W500–502.

Hiltonen, T., Björkbacka, H., Forsman, C., Clarke, A.K., Samuelsson, G., 1998. Intracellular beta-carbonic anhydrase of the unicellular green alga *Coccomyxa*. Cloning of the cdna and characterization of the functional enzyme overexpressed in *Escherichia coli*. Plant Physiol. 117, 1341–1349.

Hoffmann, K.M., Million-Perez, H.R., Merkhofer, R., Nicholson, H., Rowlett, R.S., 2015. Allosteric reversion of *Haemophilus influenzae* beta-carbonic anhydrase via a proline shift. Biochemistry 54, 598–611.

Huang, S., Hainzl, T., Grundström, C., Forsman, C., Samuelsson, G., Sauer-Eriksson, A.E., 2011. Structural studies of beta-carbonic anhydrase from the green alga *Coccomyxa*: inhibitor complexes with anions and acetazolamide. PLoS ONE 6, e28458.

Iverson, T.M., Alber, B.E., Kisker, C., Ferry, J.G., Rees, D.C., 2000. A closer look at the active site of gamma-class carbonic anhydrases: high-resolution crystallographic studies of the carbonic anhydrase from *Methanosarcina thermophila*. Biochemistry 39, 9222–9231.

Kikutani, S., Nakajima, K., Nagasato, C., Tsuji, Y., Miyatake, A., Matsuda, Y., 2016. Thylakoid luminal theta-carbonic anhydrase critical for growth and photosynthesis in the marine diatom *Phaeodactylum tricornutum*. Proc. Natl. Acad. Sci. U.S.A. 113, 9828–9833.

Kim, S., Yeon, J., Sung, J., Jin, M.S., 2020. Crystal structure of β-carbonic anhydrase CafA from the fungal pathogen *Aspergillus fumigatus*. Mol. Cells 43, 831–840.

Kimber, M.S., Pai, E.F., 2000. The active site architecture of *Pisum sativum* beta-carbonic anhydrase is a mirror image of that of alpha-carbonic anhydrases. EMBO J. 19, 1407–1418.

Klengel, T., Liang, W.J., Chaloupka, J., Ruoff, C., Schröppel, K., Naglik, J.R., Eckert, S.E., Mogensen, E.G., Haynes, K., Tuite, M.F., Levin, L.R., Buck, J., Mühlschlegel, F.A., 2005. Fungal adenylyl cyclase integrates CO_2 sensing with cAMP signaling and virulence. Curr. Biol. 15, 2021–2026.

Klomsiri, C., Karplus, P.A., Poole, L.B., 2011. Cysteine-based redox switches in enzymes. Antioxid. Redox Signal. 14, 1065–1077.

Latgé, J.P., 1999. *Aspergillus fumigatus* and aspergillosis. Clin. Microbiol. Rev. 12, 310–350.

Lehneck, R., Neumann, P., Vullo, D., Elleuche, S., Supuran, C.T., Ficner, R., Pöggeler, S., 2014. Crystal structures of two tetrameric beta-carbonic anhydrases from the filamentous ascomycete *Sordaria macrospora*. FEBS J. 281, 1759–1772.

Marques, J.R., da, R.R., Fonseca, Drury, B., Melo, A., 2010. Amino acid patterns around disulfide bonds. Int. J. Mol. Sci. 11, 4673–4686.

Maupin, C.M., Voth, G.A., 2007. Preferred orientations of His64 in human carbonic anhydrase II. Biochemistry 46, 2938–2947.

McCoy, A.J., Grosse-Kunstleve, R.W., Adams, P.D., Winn, M.D., Storoni, L.C., Read, R.J., 2007. Phaser crystallographic software. J. Appl. Crystallogr. 40, 658–674.

McGurn, L.D., Moazami-Goudarzi, M., White, S.A., Suwal, T., Brar, B., Tang, J.Q., Espie, G.S., Kimber, M.S., 2016. The structure, kinetics and interactions of the beta-carboxysomal beta-carbonic anhydrase, CcaA. Biochem. J. 473, 4559–4572.

Meldrum, N.U., Roughton, F.J., 1933. Carbonic anhydrase. Its preparation and properties. J. Physiol. 80, 113–142.

Mikulski, R.L., Silverman, D.N., 2010. Proton transfer in catalysis and the role of proton shuttles in carbonic anhydrase. Biochim. Biophys. Acta, Gene Struct. Expression 1804, 422–426.

Mitsuhashi, S., Mizushima, T., Yamashita, E., Yamamoto, M., Kumasaka, T., Moriyama, H., Ueki, T., Miyachi, S., Tsukihara, T., 2000. X-ray structure of beta-carbonic anhydrase from the red alga, *Porphyridium purpureum*, reveals a novel catalytic site for CO_2 hydration. J. Biol. Chem. 275, 5521–5526.

Mogensen, E.G., Janbon, G., Chaloupka, J., Steegborn, C., Fu, M.S., Moyrand, F., Klengel, T., Pearson, D.S., Geeves, M.A., Buck, J., Levin, L.R., Mühlschlegel, F.A., 2006. *Cryptococcus neoformans* senses CO_2 through the carbonic anhydrase Can2 and the adenylyl cyclase Cac1. Eukaryot. Cell 5, 103–111.

Mullins, J., Harvey, R., Seaton, A., 1976. Sources and incidence of airborne *Aspergillus fumigatus* (Fres). Clin Allergy 6, 209–217.

Murshudov, G.N., Vagin, A.A., Dodson, E.J., 1997. Refinement of macromolecular structures by the maximum-likelihood method. Acta Crystallogr. D Biol. Crystallogr. 53, 240–255.

Neish, A.C., 1939. Studies on chloroplasts: their chemical composition and the distribution of certain metabolites between the chloroplasts and the remainder of the leaf. Biochem. J. 33, 300–308.

Nienaber, L., Cave-Freeman, E., Cross, M., Mason, L., Bailey, U.M., Amani, P., R, A.D., Taylor, P., Hofmann, A., 2015. Chemical probing suggests redox-regulation of the carbonic anhydrase activity of mycobacterial Rv1284. FEBS J 282, 2708-2721.

Otwinowski, Z., Minor, W., 1997. Processing of X-ray diffraction data collected in oscillation mode. Methods Enzymol. 276, 307–326.

Pace, N.J., Weerapana, E., 2014. Zinc-binding cysteines: diverse functions and structural motifs. Biomolecules 4, 419–434.

Paulsen, C.E., Carroll, K.S., 2010. Orchestrating redox signaling networks through regulatory cysteine switches. ACS Chem. Biol. 5, 47–62.

Pfaller, M.A., Diekema, D.J., 2010. Epidemiology of invasive mycoses in North America. Crit. Rev. Microbiol. 36, 1–53.

Ren, P., Chaturvedi, V., Chaturvedi, S., 2014. Carbon dioxide is a powerful inducer of monokaryotic hyphae and spore development in *Cryptococcus gattii* and carbonic anhydrase activity is dispensable in this dimorphic transition. PLoS ONE 9.
Rowlett, R.S., 2010. Structure and catalytic mechanism of the beta-carbonic anhydrases. Biochim. Biophys. Acta, Gene Struct. Expression 1804, 362–373.
Rowlett, R.S., Hoffmann, K.M., Failing, H., Mysliwiec, M.M., Samardzic, D., 2010. Evidence for a bicarbonate "escort" site in *Haemophilus influenzae* beta-carbonic anhydrase. Biochemistry 49, 3640–3647.
Rowlett, R.S., Tu, C., McKay, M.M., Preiss, J.R., Loomis, R.J., Hicks, K.A., Marchione, R. J., Strong, J.A., Donovan Jr., G.S., Chamberlin, J.E., 2002. Kinetic characterization of wild-type and proton transfer-impaired variants of beta-carbonic anhydrase from *Arabidopsis thaliana*. Arch. Biochem. Biophys. 404, 197–209.
Rumeau, D., Cuiné, S., Fina, L., Gault, N., Nicole, M., Peltier, G., 1996. Subcellular distribution of carbonic anhydrase in *Solanum tuberosum* L. leaves: characterization of two compartment-specific isoforms. Planta 199, 79–88.
Schlicker, C., Hall, R.A., Vullo, D., Middelhaufe, S., Gertz, M., Supuran, C.T., Mühlschlegel, F.A., Steegborn, C., 2009. Structure and inhibition of the CO_2-sensing carbonic anhydrase Can2 from the pathogenic fungus *Cryptococcus neoformans*. J. Mol. Biol. 385, 1207–1220.
Shaban, N.M., Shi, K., Li, M., Aihara, H., Harris, R.S., 2016. 1.92 Angstrom zinc-free APOBEC3F catalytic domain crystal structure. J. Mol. Biol. 428, 2307–2316.
Smith, K.S., Ferry, J.G., 1999. A plant-type (beta-class) carbonic anhydrase in the thermophilic methanoarchaeon *Methanobacterium thermoautotrophicum*. J. Bacteriol. 181, 6247–6253.
Smith, K.S., Jakubzick, C., Whittam, T.S., Ferry, J.G., 1999. Carbonic anhydrase is an ancient enzyme widespread in prokaryotes. Proc. Natl. Acad. Sci. U.S.A. 96, 15184–15189.
Steinbach, W.J., Marr, K.A., Anaissie, E.J., Azie, N., Quan, S.P., Meier-Kriesche, H.U., Apewokin, S., Horn, D.L., 2012. Clinical epidemiology of 960 patients with invasive aspergillosis from the PATH Alliance registry. J. Infect. 65, 453–464.
Strop, P., Smith, K.S., Iverson, T.M., Ferry, J.G., Rees, D.C., 2001. Crystal structure of the "cab"-type beta class carbonic anhydrase from the archaeon *Methanobacterium thermoautotrophicum*. J. Biol. Chem. 276, 10299–10305.
Suarez Covarrubias, A., Larsson, A.M., Högbom, M., Lindberg, J., Bergfors, T., Björkelid, C., Mowbray, S.L., Unge, T., Jones, T.A., 2005. Structure and function of carbonic anhydrases from *Mycobacterium tuberculosis*. J. Biol. Chem. 280, 18782–18789.
Supuran, C.T., 2008. Carbonic anhydrases: novel therapeutic applications for inhibitors and activators. Nat. Rev. Drug Discov. 7, 168–181.
Supuran, C.T., 2016. Structure and function of carbonic anhydrases. Biochem. J. 473, 2023–2032.
Teng, Y.-B., Jiang, Y.-L., He, Y.-X., He, W.-W., Lian, F.-M., Chen, Y., Zhou, C.-Z., 2009. Structural insights into the substrate tunnel of *Saccharomyces cerevisiae* carbonic anhydrase Nce103. BMC Struct. Biol. 9, 67.
Tripp, B.C., Ferry, J.G., 2000. A structure-function study of a proton transport pathway in the gamma-class carbonic anhydrase from *Methanosarcina thermophila*. Biochemistry 39, 9232–9240.
Kisiel, W., Graf, G., 1972. Purification and characterization of carbonic anhydrase from *Pisum sativum*. Phytochemistry 11, 113–117.
Xu, Y., Feng, L., Jeffrey, P.D., Shi, Y., Morel, F.M., 2008. Structure and metal exchange in the cadmium carbonic anhydrase of marine diatoms. Nature 452, 56–61.